



HAL
open science

Mapping spin–charge conversion to the band structure in a topological oxide two-dimensional electron gas

Diogo Vaz, Paul Noël, Annika Johansson, Börge Göbel, Flavio Bruno,
Gyanendra Singh, Siobhan Mckeown-Walker, Felix Trier, Luis Vicente-Arche,
Anke Sander, et al.

► To cite this version:

Diogo Vaz, Paul Noël, Annika Johansson, Börge Göbel, Flavio Bruno, et al.. Mapping spin–charge conversion to the band structure in a topological oxide two-dimensional electron gas. *Nature Materials*, 2019, 10.1038/s41563-019-0467-4 . hal-02288886

HAL Id: hal-02288886

<https://hal.science/hal-02288886>

Submitted on 7 May 2020

HAL is a multi-disciplinary open access archive for the deposit and dissemination of scientific research documents, whether they are published or not. The documents may come from teaching and research institutions in France or abroad, or from public or private research centers.

L'archive ouverte pluridisciplinaire **HAL**, est destinée au dépôt et à la diffusion de documents scientifiques de niveau recherche, publiés ou non, émanant des établissements d'enseignement et de recherche français ou étrangers, des laboratoires publics ou privés.

Mapping spin-charge conversion to the band structure in a topological oxide two-dimensional electron gas

Diogo C. Vaz^{1*}, Paul Noël^{2*}, Annika Johansson^{3,4*}, Børge Göbel^{3*}, Flavio Bruno⁵, Gyanendra Singh⁶,
Siobhan McKeown-Walker⁵, Felix Trier¹, Luis M. Vicente-Arche¹, Anke Sander¹, Sergio Valencia⁷,
Pierre Bruneel⁸, Manali Vivek⁸, Marc Gabay⁸, Nicolas Bergeal⁶, Felix Baumberger⁵, Hanako Okuno⁹,
Agnès Barthélémy¹, Albert Fert¹, Laurent Vila^{2*}, Ingrid Mertig^{4,3}, Jean-Philippe Attané² and
Manuel Bibes^{1♦}

¹ Unité Mixte de Physique CNRS, Thales, Univ. Paris-Sud, Université Paris-Saclay, 91767 Palaiseau (France)

² Univ. Grenoble Alpes, CEA, CNRS, Grenoble INP, INAC-Spintec, 38000 Grenoble (France)

³ Max Planck Institute of Microstructure Physics, 06120 Halle (Germany)

⁴ Institute of Physics, Martin Luther University Halle-Wittenberg, 06099 Halle (Germany)

⁵ Department of Quantum Matter Physics, University of Geneva, 24 Quai Ernest Ansermet, 1211 Geneva (Switzerland)

⁶ Laboratoire de Physique et d'Etude des Matériaux, ESPCI Paris, PSL Research University, CNRS, 10 Rue Vauquelin, 75005, Paris (France)

⁷ Helmholtz-Zentrum Berlin für Materialien und Energie, Albert-Einstein-Strasse 15, 12489 Berlin (Germany)

⁸ Laboratoire de Physique des Solides, CNRS, Univ. Paris-Sud, Université Paris-Saclay, 91405 Orsay (France)

⁹ Univ. Grenoble Alpes, CEA, INAC-MEM, 38000 Grenoble (France)

While classical spintronics has traditionally relied on ferromagnetic metals as spin generators and spin detectors, a new approach called spin-orbitronics exploits the interplay between charge and spin currents enabled by the spin-orbit coupling (SOC) in non-magnetic systems. Efficient spin-charge interconversion can be realized through the direct and inverse Edelstein effects at interfaces where broken inversion symmetry induces a Rashba SOC. Although the simple Rashba picture of split parabolic bands is usually used to interpret such experiments, it fails to explain the largest conversion effects and their relation to the actual electronic structure. Here, we demonstrate a very large spin-to-charge conversion effect (inverse Edelstein length $\lambda_{iEE} > 20$ nm) in an interface-engineered high-carrier-density SrTiO₃ two-dimensional electron gas (2DEG) and use angle-resolved photoemission measurements and Boltzmann calculations to map its peculiar gate dependence to the band structure. We show that the conversion process is amplified by enhanced Rashba-like splitting due to orbital mixing, and in the vicinity of avoided band crossings with topologically non-trivial order. Our results indicate that oxide 2DEGs formed by a simple room-temperature sputtering procedure are strong candidates for spin-based information readout in novel memory and transistor designs. At the same time, they confirm the promise of topology as a new ingredient to expand the scope of complex oxides for spintronics.

* these authors contributed equally to this work. [✉] laurent.vila@cea.fr [♦] manuel.bibes@cnrs-thales.fr

38 The Rashba effect is a quantum phenomenon that occurs at surfaces and interfaces where spatial
39 symmetry breaking results in an out-of-plane electric field¹. In the presence of spin-orbit coupling
40 (SOC), this leads to a lifting of the spin degeneracy and a locking of the momentum and spin degrees
41 of freedom causing pairs of Fermi contours with a momentum splitting and opposite spin chiralities².
42 When a two-dimensional (2D) charge current j_c^{2D} flows in a Rashba system, it generates a transverse
43 spin density through the Edelstein effect (EE) (also called Rashba-Edelstein or inverse spin galvanic
44 effect)³. This spin density can diffuse in an adjacent conducting material through the interface,
45 generating a three-dimensional (3D) pure spin current j_s^{3D} without net charge current (that is, a pure
46 flow of spin angular momentum, with opposite flows for electrons of opposite spins). Conversely, the
47 injection of a spin current into a Rashba system generates a net charge current (inverse Edelstein
48 effect, IEE or spin galvanic effect)⁴. The EE and IEE can also be realized at surfaces of three-
49 dimensional topological insulators⁵, and have been predicted in other types of quantum materials^{6,7}.

50 The interpretation of the IEE in topological insulators is relatively simple since they usually have only
51 one Fermi contour. The figure of merit $\lambda_{IEE} = j_c^{2D}/j_s^{3D}$ is given by the product of the Fermi velocity
52 v_f and the momentum relaxation time τ (Ref. ⁸). However, the situation is more complex in Rashba
53 systems, where conversion occurs in two inequivalent Fermi contours whose contributions partially
54 compensate each other^{4,9}, so that $\lambda_{IEE} = \alpha_R \tau / \hbar$ (in the approximation of circular Fermi contours)
55 with α_R the Rashba coefficient. Unexpectedly, the largest λ_{IEE} values (6.4 nm) were not reported for
56 topological insulators but for SrTiO₃-based two-dimensional electron gases (2DEGs) with a moderate
57 effective Rashba SOC¹⁰. This unconventional result has been ascribed to the long relaxation time and
58 to the multi-orbital nature of the system^{10,11}. However, a detailed understanding is still lacking.

59 A 2DEG at the interface between SrTiO₃ (STO) and another perovskite insulator, LaAlO₃ (LAO), first
60 discovered by Ohtomo and Hwang in 2004¹², possesses many interesting attributes including low-
61 temperature superconductivity and a carrier density that is highly tunable by a gate voltage¹³. While
62 the mechanisms for 2DEG formation remain debated, it is universally found that a thickness of at
63 least four unit cells of LAO is needed for the 2DEG to appear¹⁴ (although it can be reduced by metal
64 capping^{15,16}). Beyond this threshold, the properties of the 2DEG vary little with LAO thickness. Very
65 recently, Rödel et al. reported that a 2DEG could also be formed in STO through the deposition of a
66 few Å of Al at room temperature¹⁷. This approach has several advantages as it alleviates the need for
67 the high temperature growth of crystalline LAO and allows the modulation of the carrier density over
68 a broader range, through the adjustment of the Al thickness or the use of other metals¹⁸. Here, we
69 report a very large inverse Edelstein effect in such Al/STO 2DEGs. The conversion efficiency and its
70 sign strongly depend on the gate voltage, with λ_{IEE} reaching values in the range of ± 20 nm. We
71 quantitatively relate these values to the Fermi-energy-dependent Edelstein effect calculated within

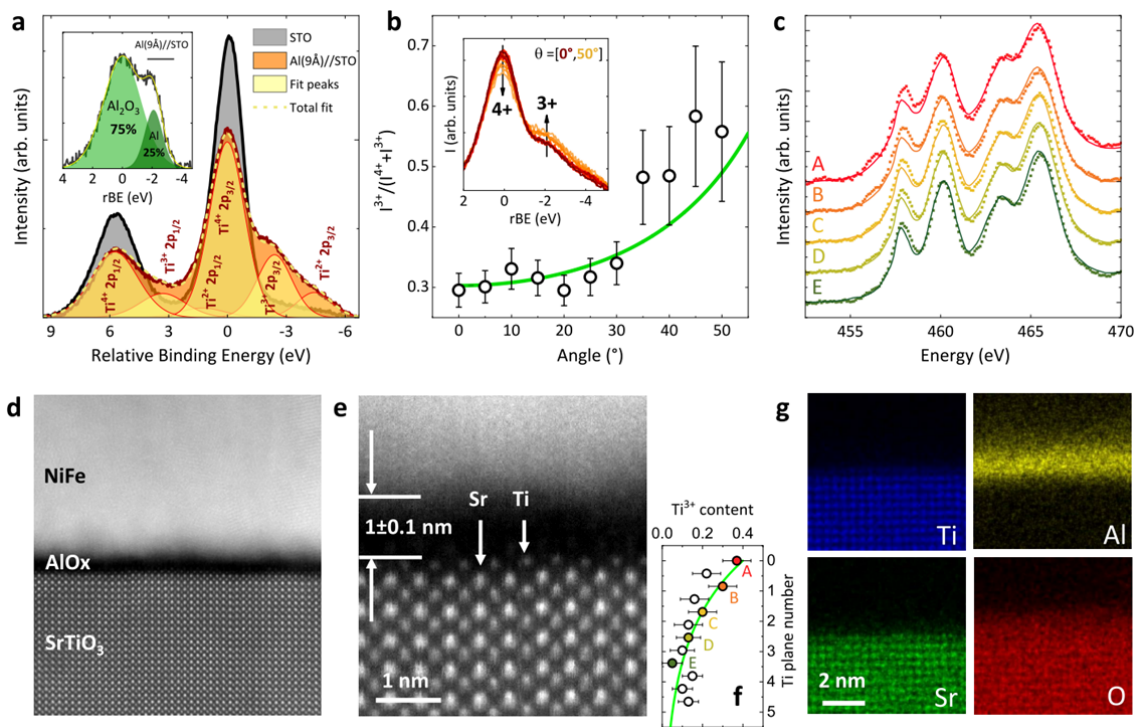
72 the semi-classical Boltzmann transport theory applied to the experimentally determined electronic
73 structure.

74 Following Ref. ¹⁷ we prepared STO 2DEGs by depositing an ultra-thin layer of Al (nominal thickness
75 9 Å) on TiO₂-terminated STO substrates using magnetron sputtering (see Methods). For scanning
76 transmission electron microscopy (STEM), magnetotransport and spin-pumping experiments, we
77 grew an additional NiFe layer and an AlO_x cap (3 nm in thickness) in the same vacuum cycle. The NiFe
78 thickness was 2.5 nm for transport and 20 nm for STEM and spin-pumping. To evaluate the
79 interaction between Al and the first few layers of STO, we performed in situ X-ray photoelectron
80 spectroscopy (XPS) experiments focusing on the Ti 2p and Al 2p states (Fig. 1a). The spectrum
81 collected for a bare STO substrate (grey area) corresponds to a Ti⁴⁺ valence state, consistent with its
82 insulating character. Upon deposition of the ultrathin Al layer, two peaks associated with Ti³⁺ and Ti²⁺
83 valence states arise, pointing to the reduction of the STO and the generation of an electron-rich layer
84 at its interface with Al. The spectral weight of these peaks is larger than normally observed in
85 LAO/STO heterostructures^{16,19}, indicating a higher electron density. In the inset, we see that the Al 2p
86 signal comprises two spectral features, corresponding to oxidized and metallic Al (high and low
87 binding energies, respectively) and suggesting that the Al is largely oxidized. As previously reported¹⁷,
88 we conclude that Al is able to react with the surface oxygens and thus induces oxygen vacancies
89 acting as electron donors in the first few layers of STO. From here on we thus refer to these samples
90 as AlO_x/STO.

91 We have also characterized the interface by cross sectional STEM analysis. As seen in the Z-contrast
92 in high-angle annular dark field (HAADF) images of Figures 1d and 1e, a continuous Al-rich layer can
93 be identified, between the TiO₂-terminated SrTiO₃ surface and the NiFe layer, with a uniform
94 thickness over all observed areas in the STEM specimen. The AlO_x thickness estimated using HAADF Z
95 contrast is 1.0±0.1 nm, consistent with the deposition of 0.9 nm of Al metal and its volume expansion
96 upon oxidation. Sr, Ti, Al and O elemental chemical maps have been acquired using electron
97 dispersive X-ray spectroscopy (EDX), and show that oxygen is present in STO but also extends
98 through the Al layer. A tiny amount of Ti also appears to be present in the Al-rich region. Overall, the
99 STEM analysis corroborates the XPS data and clearly evidences that the Al layer is oxidized at the STO
100 interface.

101 To estimate the spatial distribution of the Ti³⁺-rich layer, we performed angle-dependent XPS
102 experiments (cf. Fig. 1b) and electron energy loss spectroscopy (EELS) at the Ti L_{3,2} edge (cf. Fig. 1c).
103 EELS data in the Al-rich region (see Supplementary Material) suggest that most of the Ti²⁺ seen in XPS
104 is found within the Al-rich layer. In Fig. 1b, we plot the ratio between the weights of the Ti³⁺ and Ti⁴⁺

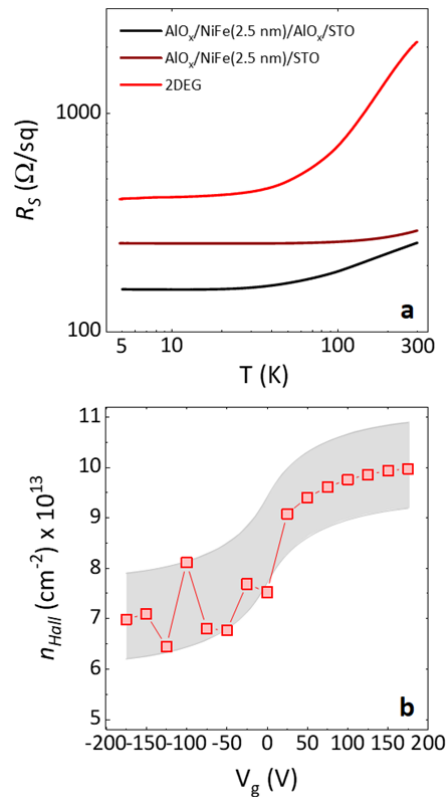
105 peaks, that increases exponentially with the XPS electron take-off angle, indicating a larger
 106 concentration of Ti^{3+} closer to the interface. The data are well fitted using a depth-profile model,
 107 previously used to estimate the thickness of 2DEG in LAO/STO samples¹⁹. We extract a total electron
 108 density of $7.2 \pm 1.0 \times 10^{14} \text{ cm}^{-2}$ and a thickness of $1.4 \pm 0.4 \text{ nm}$, confirming the quasi 2D nature of the
 109 electron gas. The mixed valence of Ti in STO is also seen in the EELS data presented in Fig. 1c, that we
 110 simulated with linear combinations of Ti^{3+} and Ti^{4+} reference signals (taking into account the
 111 experimental resolution). The extracted Ti^{3+} content is plotted in Fig. 1f, and is found to decrease
 112 when going deeper into the STO. The total Ti^{3+} concentration corresponds to an electron density of
 113 $6.3 \pm 1.0 \times 10^{14} \text{ cm}^{-2}$, consistent with the XPS analysis.



114

115 **Figure 1. Characterization of AlO_x/STO 2DEGs.** (a) X-ray photoelectron spectra near the Ti 2p state
 116 for a STO single crystal before (black) and after (red) deposition of 9 Å of Al. Inset: spectrum at the Al
 117 2p state after deposition of 9 Å of Al on STO; rBE stands for relative binding energy. (b) Ti^{3+} fraction
 118 for different take-off angles. The error bars come from the fitting process using CasaXPS (see
 119 Methods). The experimental spectra are shown in the inset. The green line is a fit using the model of
 120 Ref. ¹⁹. (c) EELS spectra at positions indicated in (f) in SrTiO₃ (dotted) with simulations (lines) using
 121 linear combinations of Ti^{3+} and Ti^{4+} spectra corrected for instrumental resolution. (d) Scanning
 122 transmission electron microscopy image. (e) Magnified view of (d). (f) Variation of the Ti^{3+} content
 123 deduced from simulations shown in (c) as a function of position in SrTiO₃. The green line is an
 124 exponential fit. (g) EDX maps.

125 We now turn to the transport properties. The temperature dependence of the sheet resistance for a
 126 $\text{AlO}_x/\text{NiFe}/\text{AlO}_x/\text{STO}$ sample and a $\text{AlO}_x/\text{NiFe}/\text{STO}$ reference sample is displayed in Fig. 2a. Without
 127 the Al insertion (brown curve), the resistance shows practically no change over the whole range of
 128 temperatures. In contrast, in the full stack (black curve) a drop in resistance is observed below 100 K,
 129 signalling an additional conduction path corresponding to the 2DEG. The red curve represents the
 130 isolated 2DEG contribution, deduced through a two-channel parallel conduction model¹⁶. Hall traces
 131 of the 2DEG were extracted¹⁶ from Hall measurements at $T = 7$ K while applying a back-gate voltage
 132 V_g . While a non-linear Hall signal was obtained for large positive gate voltages, decreasing V_g
 133 promoted a more linear dependence, suggesting that a transition between multi-band and single-
 134 band transport occurs. Fitting the Hall traces in the linear regime and using capacitance
 135 measurements²⁰ we obtained the mobile carrier densities in both regimes. As visible in Fig. 2b, the
 136 carrier density varies from about $7 \times 10^{13} \text{ cm}^{-2}$ at -175 V to $1 \times 10^{14} \text{ cm}^{-2}$ at $+175$ V. We note that, as
 137 often reported in STO 2DEGs, the density of mobile carriers is significantly lower than the total
 138 electron concentration inferred from core level spectroscopy¹⁹, suggesting the existence of a large
 139 fraction of localized electrons.

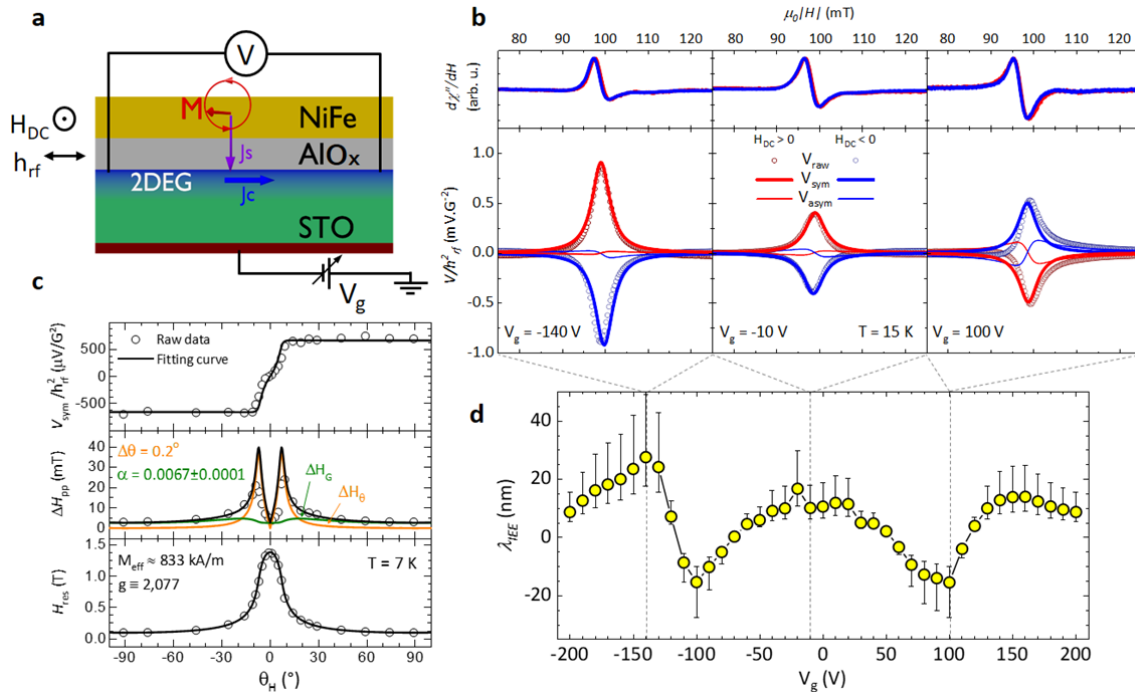


140

141 **Figure 2. Magnetotransport properties.** (a) Temperature dependence of the sheet resistance of a
 142 $\text{AlO}_x/\text{NiFe}/\text{AlO}_x/\text{STO}$ sample (black) and a $\text{AlO}_x/\text{NiFe}/\text{STO}$ reference sample, with a deposited Al

143 thickness of 9 Å (brown). The extracted contribution from the 2DEG is shown in red. (b) Carrier density
 144 as a function of gate voltage. The shaded area, derived from the capacitance measurement,
 145 corresponds to the uncertainty in the determination of n_{Hall} .

146 To characterize the IEE in our AlO_x/STO 2DEGs, we used spin pumping ferromagnetic resonance
 147 (FMR) experiments at 15 K on a $\text{AlO}_x/\text{NiFe}(20 \text{ nm})/\text{AlO}_x/\text{STO}$ sample with a nominal deposited Al
 148 thickness of 9 Å (see Methods). Fig. 3a depicts the principle of the technique: DC and radio frequency
 149 (rf) magnetic fields H_{DC} and h_{rf} are applied to excite magnetization precession in the NiFe layer. At
 150 ferromagnetic resonance, a pure spin current is injected in the 2DEG²¹. In the presence of IEE, a
 151 transverse DC voltage will be generated. Fig. 3b shows FMR signals (top panels) at different gate
 152 voltages. The FMR resonance field and the linewidth do not vary, implying that the gate voltage does
 153 not affect the properties of the ferromagnet. The bottom panels of Fig. 3b show the voltage signals
 154 produced at resonance, possessing two components: a symmetric one and a much smaller
 155 antisymmetric one (V_{sym} and V_{asym} respectively), both of which are reversed upon reversing H_{DC} .
 156 While the antisymmetric component arises from spin rectification effects such as anisotropic
 157 magnetoresistance, the symmetric component (spin signal) is due to spin-charge conversion (by
 158 inverse spin Hall effect – ISHE – or IEE). For all gate voltages shown, V_{sym} strongly dominates the
 159 signal, pointing to a high spin-charge conversion efficiency. In addition, the signal was observed to be
 160 linear with the rf power, for a maximum of 5 mW.



161
 162 **Figure 3. Spin-charge conversion in NiFe/AlO_x/STO.** (a) Sketch of the spin pumping experiment. (b)
 163 FMR curves (top) and spin signals (bottom) for different values of the gate voltage, for a positive (red)

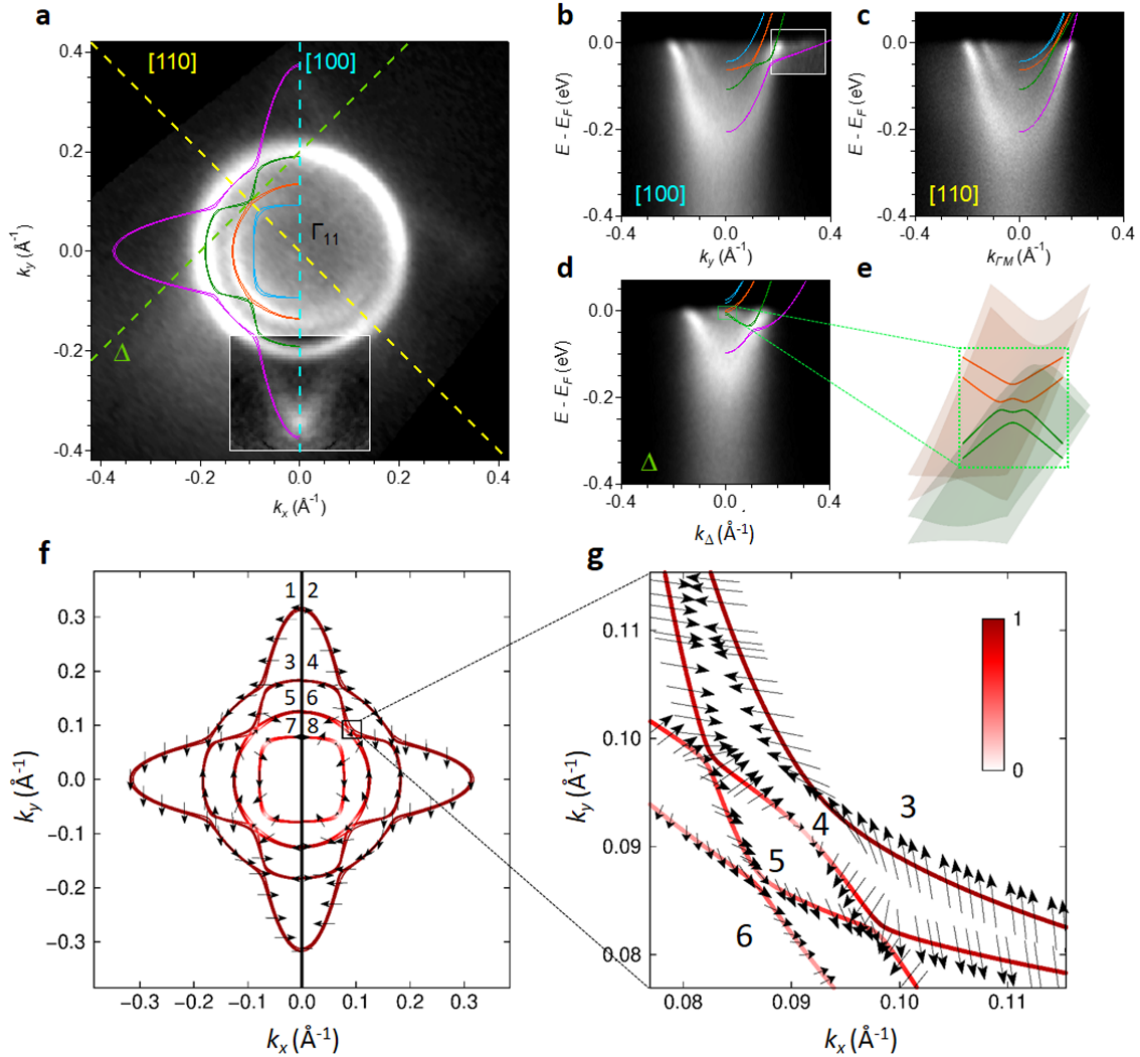
164 and negative (blue) applied DC magnetic field. The symmetric V_{sym} and antisymmetric V_{asym}
 165 components of the raw spin signals V_{raw} are represented using continuous thick and thin lines,
 166 respectively. (c) Top panel: angular out-of-plane dependence of the amplitude of the symmetric
 167 component of the spin-pumping signal, normalized by the square of the applied rf field. Center panel:
 168 angular out-of-plane dependence of the ferromagnetic resonance peak-to-peak linewidth. The fit
 169 enables the separation of the contributions of the damping (ΔH_G) and the magnetic inhomogeneities
 170 in the FM layer (ΔH_θ), thus allowing the extraction of the damping parameter α . Bottom panel:
 171 angular out-of-plane dependence of the ferromagnetic resonance field. The fit allows the extraction
 172 of the magnetization and g-factor. All the fits have been made using the model proposed in Ref.²² (d)
 173 Spin-charge conversion efficiency λ_{IEE} as a function of gate voltage at 15 K. The error bars come from
 174 the uncertainty in the determination of the spin mixing conductance (see Supplementary Material).

175 The out-of-plane angular dependence of the spin signal amplitude, shown in Fig. 3c, is in agreement
 176 with the theoretical expectations for ISHE or IEE²². The out-of-plane angular dependences of the
 177 ferromagnetic resonance peak-to-peak linewidth ΔH_{pp} and the ferromagnetic resonance field H_{res}
 178 allow the extraction of the magnetization $M_{eff}=833 \text{ kA}\cdot\text{m}^{-1}$, the g-factor $g=2.077$ and the damping
 179 $\alpha=0.0066$ that are typical of a 20 nm thick NiFe film.

180 The value of j_S^{3D} can then be calculated by comparing the value of α with that of a reference NiFe/Si
 181 sample²¹; the spin mixing conductance was $G_{eff}^\uparrow=2.2\pm 1 \text{ nm}^{-2}$ (see Supplementary Material). j_C^{2D} can
 182 be extracted from the spin signal value and the sample resistivity⁴. From j_S^{3D} and j_C^{2D} we calculate
 183 λ_{IEE} and plot its gate dependence in Fig. 3d. The spin-charge conversion varies strongly in sign and
 184 amplitude, with its sign changing several times in the studied range of gate voltages. Moreover, the
 185 conversion efficiencies at maximum values are extremely high, for both positive and negative values
 186 (+28 nm, -16 nm). These efficiencies are, in absolute value, much higher than those measured in
 187 other spin-orbit systems. In spin Hall materials, λ_{IEE} can be compared to the product of the spin Hall
 188 angle and the spin diffusion length, and typical values are below 1 nm for Pt or W²³. In topological
 189 insulators, λ_{IEE} values go up to 2.1 nm in α -Sn (Ref. ⁵), 2.0 nm in HgTe (Ref. ²⁴), and 0.08 nm in (Bi,
 190 Sb)Te (Ref. ²⁵). The conversion efficiency observed here is also higher than what can be obtained in
 191 Rashba interfaces (0.3 nm in Ag/Bi, Ref. ⁴), or even in previously studied oxide-based systems (6.4 nm
 192 in LAO/STO, Ref. ¹⁰, and 0.6 nm in Cu/Bi₂O₃, Ref. ²⁶).

193 To gain more insight into the relationship between the IEE effect and the electronic structure of STO
 194 2DEGs, we have performed angle-resolved photoemission experiments on Al/STO and vacuum-
 195 cleaved STO samples with integrated carrier densities in the 10^{13} - 10^{14} cm^{-2} range (see Supplementary
 196 Material). Fig. 4a displays the ARPES Fermi surface of a 2DEG stabilized at the (001) surface of STO for

197 a sample with $n \approx 1.5 \times 10^{14} \text{ cm}^{-2}$. In bulk STO, d_{xy} , d_{yz} , and d_{zx} bands near the Fermi energy are
 198 hybridized due to spin-orbit interaction. The confinement in the 2DEG leads to the creation of sub-
 199 bands and the emergence of an unconventional Rashba effect with a spin splitting that is enhanced
 200 in certain k -space areas²⁷⁻²⁹ due to orbital mixing. We resolve three concentric circular contours
 201 centred at the Γ_{11} point and two ellipsoidal Fermi surface sheets with major axes along the k_x and k_y
 202 direction, respectively, giving four inequivalent bands in total (two heavy and two light bands),
 203 consistent with previous studies^{17,27,30}. The ellipsoidal features have lower intensity due to the light
 204 polarization chosen for this experiment²⁷. Electronic structure dispersion plots along the high
 205 symmetry directions Γ -X [100] and Γ -M [110] are displayed in Figures 4b and 4c respectively. In the
 206 dispersion plot along Δ , shown in Figure 4d, we resolve the lowest lying sub-band that forms the
 207 outer Fermi surface sheet. In addition, we observe additional spectral weight at $k_{\Delta}=0$ located ~ 15
 208 meV below the Fermi level (see Supplementary Material).



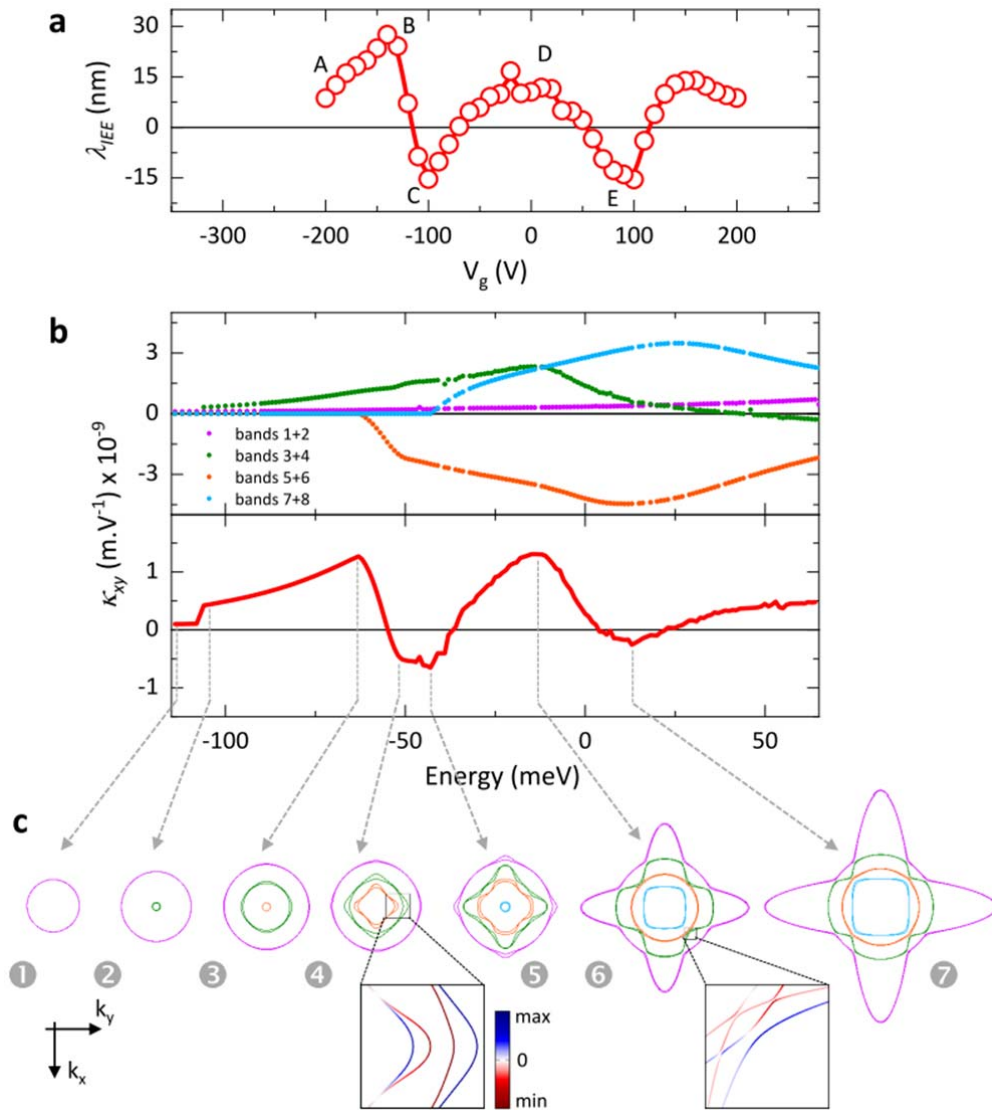
209

210 **Figure 4. Electronic and spin structure of the 2DEG.** (a) Experimental Fermi surface of the 2DEG
 211 around the Γ_{11} point. (b) Band dispersion along the [100] direction – cf. cyan dashed line in (a), with
 212 overlaid bands calculated by an eight-band tight-binding model. (c) Same along the [110] direction –
 213 cf. yellow dashed line in (a). The insets to (a,b) use an enhanced contrast to better visualize the faint
 214 heavy bands (see Methods). (d) Same along the Δ direction – cf. green dashed line in (a). (e)
 215 Calculated band structure along Δ near k_c . (f) Calculated Fermi surface and spin expectation values
 216 (direction: arrows, absolute value: color scale) at an energy near the band inversion region, where the
 217 left (right) panel corresponds to the outer (inner) band of each pair. The numbers denote the band in
 218 energetically ascending order. (g) is a zoom-in near k_c (boxed region in f).

219 Next, we derive a model Hamiltonian that reproduces the ARPES measurements. We take into
 220 account the two energetically lowest d_{xy} bands and one d_{yz} and d_{zx} band, respectively. Accounting for
 221 spin, this results in an eight-band effective Hamiltonian (see Methods), which reproduces the
 222 measured ARPES band structure very well (Fig. 4a-d). Fig. 4e shows the calculated band structure
 223 along a Δ direction (perpendicular to the [110] direction). Because of the interplay between spin-
 224 orbit coupling and orbital mixing, the band structure shows a band inversion with an avoided
 225 crossing at the critical k point k_c (corresponding to $k_{\Delta}=0$). This band inversion renders the 2DEG
 226 topologically non-trivial and gives rise to spin-polarized topological edge states that have been
 227 predicted in Ref.³¹ by means of the Z_2 topological invariant. Figs. 4f and 4g show the spin expectation
 228 value for all eight bands. The band inversion discussed in Fig. 4d and 4e leads to strong modulations
 229 of the spin expectation values near the Fermi energy. Indeed, as observed in Fig. 4g, the spin
 230 expectation value almost vanishes in the fourth band near k_c , while it remains considerable in the
 231 third band, leading to uncompensated spin textures.

232 Let us now examine how this peculiar band structure produces spin-charge interconversion. We
 233 characterize the direct Edelstein effect efficiency by the tensor $\hat{\kappa}$ that relates the spin \mathbf{s} per surface
 234 unit cell to the externally applied electric field \mathbf{E} , $\mathbf{s} = \hat{\kappa}\mathbf{E}$. In Fig. 5b, we plot the direct Edelstein
 235 efficiency κ_{xy} calculated from the spin expectation values for different Fermi energies (assuming a
 236 rigid band shift) using a semi-classical Boltzmann approach (see Methods). Since the EE is the
 237 Onsager reciprocal of the inverse Edelstein effect⁹ (in the approximation of transparent interfaces),
 238 the experimental data of Fig. 3d (that we replot in Fig. 5a) can be compared with the theoretical
 239 results. At low energy, only the two low-lying d_{xy} sub-bands (❶ in Fig. 5c) are occupied and κ_{xy} is
 240 relatively small, consistent with the modest Rashba-like splitting of these bands. Upon increasing
 241 energy, a step occurs corresponding to the population of the next d_{xy} sub-band pair (❷) followed by
 242 an extremum signaling the onset of the first heavy sub-band pair (❸). Then, κ_{xy} decreases and

243 changes sign, owing to the alternating sign of the spin splitting between the d_{xy} and the first pair of
 244 $d_{zx,yz}$ bands^{29,32} (as discussed in Ref.¹¹), reaching a large negative value corresponding to the trivial
 245 avoided crossing (④), i.e. the first crossing between light d_{xy} and heavy $d_{zx,yz}$ bands where orbital
 246 mixing enhances Rashba splitting²⁷. Another extremum followed by a slope change of κ_{xy} occurs at
 247 the band edge of the second pair of $d_{zx,yz}$ bands, again due to opposite spin splitting compared to the
 248 fifth and sixth bands (⑤), as seen in the light blue curve of Fig. 5b (top panel). Upon further
 249 increasing energy, the topological band inversion is reached (⑥) where the uncompensated spin
 250 texture between the third and fourth bands causes a pronounced maximum in the Edelstein signal.
 251 This large spin-charge conversion efficiency is a consequence of the *topological order* in the system.
 252 We point out, however, that it is not caused by topological edge states themselves, whose
 253 contributions would compensate at opposite edges of the 2DEG.



254

255 **Figure 5. Energy dependence of the spin-charge conversion.** (a) Gate dependence of λ_{IEE} at 15 K. (b)
 256 Energy dependence of the Edelstein tensor (top: band-resolved; bottom: total). (c) Fermi lines at
 257 various energies. ❶ Rashba-like bands 1+2. ❷ Edge of bands 3+4. ❸ Edge of bands 5+6. ❹ Trivial
 258 avoided crossing. ❺ Edge of bands 7+8. ❻ Topologically non-trivial avoided crossing (with band
 259 inversion). ❼ Maximum from multiple bands. The colour scale of the zoom-in regions in ❹ and ❻
 260 corresponds to the contribution of each state to the Edelstein effect.

261 While the trivial avoided crossing in the [100] direction (❹) unlocks only an enhanced Rashba spin
 262 splitting due to orbital mixing, the topologically non-trivial avoided crossing in the Δ direction adds a
 263 large contribution from the uncompensated spin texture (see both insets of Fig. 5c), which drives the
 264 overall Edelstein effect to large values in this region. This can be better understood by recalling the
 265 nature of the Edelstein effect in a Rashba system, where the net spin-charge current produced arises
 266 from the inequivalence of the Fermi contours. If the spin splitting between bands is larger, i.e. if
 267 Fermi contours have very different sizes, this inequivalence is enhanced. A similar result is intuitively
 268 obtained if the spin-split bands have uncompensated spin textures, where the spin current produced
 269 through the EE by one contour would be much larger than the one produced by its Rashba-split
 270 counterpart. Lastly, for even higher energy, another sign change occurs followed by a negative
 271 extremum, resulting from the competing contributions from multiple bands (❼).

272 Remarkably, the calculated κ_{xy} curve qualitatively reproduces the occurrence of extrema and sign
 273 changes in the IEE signal. However, the presented energy range cannot be unambiguously related to
 274 the depicted gate voltage. To gain more insight into their correspondence, we have performed
 275 Poisson-Schrödinger calculations of the energy spectrum for an STO interface (see Supplementary
 276 Material). They indicate that to shift the Fermi level from the expected energy of the topologically
 277 avoided crossing to the trivial avoided crossing, the 2DEG needs to be depleted by $\Delta n = 2.6 \times 10^{13} \text{ cm}^{-2}$.
 278 By matching these two points in Fig. 5c (❻ and ❹) with points D and C in Fig. 5a, we observe that V_G
 279 was swept between about 0-20 V and -100 V, respectively. According to the transport data in Fig. 2b,
 280 this range of gate voltages is equivalent to a depletion of $\Delta n = 1.7 \pm 1 \times 10^{13} \text{ cm}^{-2}$, compatible with the
 281 estimation from Poisson-Schrödinger calculations.

282 Although the energy dependence of λ_{IEE} and κ_{xy} are quite comparable and can be related to the
 283 spin splittings of the band structure of the AlO_x/STO 2DEG, the explanation of the extremely large IEE
 284 signal needs another ingredient. In the theoretical description scattering is restricted to the 2DEG
 285 only. In the experiments, however, the electrons have in principle the possibility to leak out of the
 286 2DEG through a tunneling barrier (in this case, the AlO_x layer), and scatter in the metal with very
 287 short relaxation times (typically tens of fs). This can be considered as a second scattering channel^{33,34}

288 characterized by an escape time τ_{esc} through the tunneling barrier, in addition to the scattering
 289 between the STO states with characteristic time τ_{2DEG} . The two scattering channels lead to an
 290 effective relaxation time $\tau_{eff}=(\tau_{2DEG}^{-1} + \tau_{esc}^{-1})^{-1}$ that will set the efficiency of the conversion process.
 291 The strength of this second scattering channel can modify the IEE signal considerably. Long escape
 292 times would change the IEE signal only slightly and result in an optimal spin-charge conversion signal,
 293 while short escape times, as in metallic interfaces such as Ag/Bi⁴, would considerably reduce τ_{eff} and
 294 consequently the IEE signal. We can use this picture to compare the values of λ_{IEE} found in
 295 NiFe/LAO//STO samples¹⁰ and here in NiFe/AlO_x//STO. We deduce the escape times through 2 uc
 296 LAO and ~1 nm of AlO_x from their estimated resistance area (RA) product (through $\tau_{esc} = \frac{RAe^2m^*}{2\pi\hbar^2}$
 297 with RA≈10 Ω.μm² and 10⁵ Ω.μm², respectively). This leads to escape times in the ps range for 2 uc
 298 of LAO and in the 10 ns range for 1 nm of AlO_x. We see that for 2 uc of LAO τ_{esc} is comparable to or
 299 shorter than the momentum relaxation of the 2DEG τ_{2DEG} , estimated to 1-10 ps, which should lead to
 300 a reduction of λ_{IEE} compared to an isolated 2DEG. On the other hand, for the present NiFe/AlO_x/STO
 301 samples, τ_{esc} is much longer than τ_{2DEG} : the electrons will scatter within the 2DEG before having a
 302 chance to leak out to the metal. In this case, the 2DEG is well isolated from the metal by the alumina
 303 barrier, and λ_{IEE} can approach its optimum value.

304 Finally, to evaluate the application potential of our system, we have performed spin pumping
 305 experiments to determine the expected output voltage at room temperature. This quantity, given by
 306 the product of λ_{IEE} and the sheet resistance, is the figure of merit for devices and is relevant for
 307 instance for the spin transistor proposed by Intel (MESO device)³⁶. Since λ_{IEE} is proportional to the
 308 momentum relaxation time (and thus to the electron mobility) one expects a strong decrease of λ_{IEE}
 309 upon increasing the temperature, but in parallel the sheet resistivity should increase correspondingly
 310 and largely compensate this decrease. For the present heterostructure we find a considerable
 311 $\lambda_{IEE}=0.5\pm0.1$ nm at room temperature, and a sheet resistance on the order of 2.5 kΩ. The output
 312 voltage in the MESO device can be calculated from

$$V_{out} = P\lambda_{IEE}J_{supply}wR_S$$

313 with P the spin polarization, J_{supply} the supply current density and w the device width. Taking
 314 $P = 0.5$, $J_{supply} = 5\times10^{10}$ A/m² and $w = 300$ nm, we obtain $V_{out} \approx 10$ mV, just one order of
 315 magnitude lower than the targeted value of 100 mV. This has to be compared with the value of V_{out}
 316 one can estimate for a Pt film of 5 nm in thickness (t), that would have $R_S = \rho/t = 20$ Ω and an
 317 equivalent $\lambda_{IEE} = \theta_{SHE}l_{sf}$ with $\theta_{SHE} = 0.06$ the (inverse) spin Hall angle and $l_{sf} = 4$ nm the spin
 318 diffusion length, leading to $\lambda_{IEE} = 0.2$ nm. This yields $V_{out} = 0.03$ mV, i.e. two to three orders of
 319 magnitude less than with our STO 2DEG.

320 In summary, we have reported spin-charge conversion in an oxide 2DEG formed by the room-
321 temperature sputtering deposition of Al on SrTiO₃, with an efficiency about two orders of magnitude
322 larger than that of the canonical spin-orbit coupling material, Pt. We have related the amplitude of
323 the effect and its strong gate dependence to the band structure of the 2DEG, possessing trivial and
324 topological avoided crossings, and to the high tunnel resistance of the Al oxide layer. Highly-doped
325 STO-based oxide interfaces thus emerge as new members of the family of topological two-
326 dimensional materials, able to realize specific functions for spintronics devices. Our observation of a
327 finite spin-charge conversion effect at room temperature, combined with the high resistance of the
328 2DEG and the scalable room-temperature preparation process qualifies STO interfaces as very
329 promising materials for non-volatile spin logic architectures^{36,37}. More fundamentally, our results
330 should stimulate the search for topological phenomena in other oxide 2DEGs³⁸ and interfaces based
331 on elements heavier than Ti that could produce even stronger spin-charge interconversion effects
332 and possibly harbour more exotic states of matter³⁹.

333

334 **ACKNOWLEDGMENTS**

335 This work received support from the ERC Consolidator Grant #615759 “MINT”, the QUANTERA
336 project “QUANTOX”, the French ANR programme through projects OISO (ANR-17-CE24-0026-03),
337 TOPRISE (ANR-16-CE24-0017) and the Laboratoire d’Excellence LANEF (ANR-10-LEBX-51-01). MB
338 thanks the Alexander von Humboldt Foundation for supporting his stays at Martin-Luther-Universität
339 Halle. FT acknowledges support by research grant VKR023371 (SPINOX) from VILLUM FONDEN. AJ,
340 BG and IM acknowledge support by Priority Program SPP 1666 and SFB 762 of Deutsche
341 Forschungsgemeinschaft (DFG). DCV thanks the French Ministry of Higher Education and Research
342 and CNRS for financing his PhD thesis. We thank H. Jaffrès for insightful comments on tunnel escape
343 times, M. Sing for his help with XPS analysis and E. Schierle for his assistance with X-ray absorption
344 spectroscopy measurements.

345

346 **AUTHOR CONTRIBUTIONS**

347 MB proposed and supervised the study with help from LV, J-PA, AB and AF. DCV prepared the
348 samples with the help of FT and LMVA and performed XPS experiments and analysed the data with
349 AS. DCV, GS and NB measured the magnetotransport properties and analysed the results. HO
350 prepared the samples for STEM and EELS and performed the observations and spectroscopy
351 measurements. SV performed the X-ray absorption measurements and analysed the data. SMW, FYB

352 and FB performed the ARPES measurements and their analysis. PN performed the spin-pumping
353 experiments and analysed the data with DCV, LV, J-PA and MB. PB, MV and MG conducted the
354 Poisson-Schrödinger calculations. AJ and BG performed the tight-binding and Boltzmann calculations
355 under the supervision of IM, with inputs from MV, MG and MB. DCV and MB wrote the manuscript
356 with inputs from all authors. All authors discussed the results and contributed to their interpretation.

357 **DATA AND CODE AVAILABILITY STATEMENT**

358 The data that support the findings of this study are available from the corresponding author upon
359 reasonable request. The self-written code that generated the data for Figs. 4f,g and 5b,c is available
360 from AJ upon reasonable request.

361 **METHODS**

362 **Sample preparation.** NiFe and Al films were deposited at room temperature by dc magnetron
363 sputtering on TiO₂-terminated (001)-oriented STO substrates (from CrysTec GmbH). TiO₂-termination
364 was achieved through a chemical treatment, where the substrate was submerged in a buffered
365 hydrofluoric acid (NH₄F-HF 7:1) for 30 s and annealed under a rich oxygen environment at 1000 °C for
366 3 h. Prior to in situ XPS or sputtering procedures, the STO substrate was additionally annealed at 730
367 °C for 2 h under a partial oxygen pressure of 400 mbar. The deposition of the metallic layers was
368 performed under an Ar partial pressure of 4.5×10^{-4} mbar and a substrate-to-target distance of 7 cm.
369 The deposition rates of the Al ultra-thin layer (0.9 nm) and the NiFe layers (2.5 nm for transport and
370 20 nm for spin pumping experiments) was 0.1 and 0.2 nm/s, under an operating dc current of 30 and
371 80 mA, respectively. Samples used for transport and spin pumping were additionally capped with a
372 2.5 nm layer of Al, which becomes oxidized when exposed to air.

373 **X-ray photoemission spectroscopy** was performed using a non-monochromatized Mg K α source ($h\nu =$
374 1253.6 eV) on 10 mm x 10 mm STO and Al(0.9nm)/STO samples. Spectra analysis was carried out
375 with the CasaXPS software. From a previous work¹⁶, the maximum probing depth for this system is
376 estimated to be ~5 nm. The error bars displayed in the angle dependence experiments were
377 calculated through the error propagation of Ti³⁺/(Ti⁴⁺+Ti³⁺) spectral areas, obtained individually from
378 Monte Carlo simulations in CasaXPS.

379 **Scanning transmission electron microscopy** measurements have been carried out using a Cs-
380 corrected FEI Themis at 200 keV. HAADF-STEM images were acquired using a convergence semiangle
381 of 20 mrad and collecting scattering from >65 mrad. Energy dispersive X-ray spectroscopy (EDX) was
382 performed for elemental mapping using a Bruker EDX system consisting of four silicon drift
383 detectors in the Themis microscope. STEM specimens were prepared by the FIB lift-out technique
384 using a FEI dual-beam Strata 400S at 30 kV. EELS measurements were performed at 80 kV using a
385 double-aberration-corrected FEI Titan Ultimate TEM equipped with a high brightness electron source
386 and a Gatan Quantum energy filter equipped with Dual EELS. The probe corrector was used to obtain
387 a beam current of 120 pA while maintaining nanometer resolution. The core loss region was
388 recorded over the range 400–600 eV at a dispersion of 0.1 eV pixel⁻¹.

389 **Magnetotransport** measurements were performed with a PPMS system from Quantum Design after
390 bonding the samples with Al wires. The electrical contribution coming only from the 2DEG was
391 isolated using the method discussed in Ref.¹⁶. The variation of the carrier density n_{2D} is obtained by
392 integrating the gate capacitance $C_g(V_g)$ measured by a standard lock-in technique, over the gate
393 voltage range: $n_{2D} = n_{2D}(V_g < 0 V) + \frac{1}{eA} \int_{-175 V}^{V_g} C_g(V) dV$ where A is the area of the sample and

394 $n_{2D}(V_g < 0 V)$ is matched to the maximum and minimum Hall carrier densities experimentally
 395 obtained in the underdoped regime.

396 **Spin Pumping.** The spin-pumping experiments were carried out using a Bruker ESP300E X-band CW
 397 spectrometer at 9.68 GHz, with a loop-gap Bruker ER 4118X-MS5 cavity, and using a microwave
 398 power of 5 mW or less to remain in the linear regime. The generated DC voltage was measured using
 399 a Keithley 2182A nanovoltmeter. The gate voltage was applied using a Keithley 2400 sourcemeter.
 400 The sample was initialized by sweeping the back-gate voltage from +200 V to -200 V, and then back
 401 to +200 V, to avoid any hysteretic behavior. The measurement was then performed for different gate
 402 voltages, from +200V to -200V.

403 **Angle-resolved photoemission.** ARPES measurements were performed at the SIS beamline of the
 404 Swiss Light Source. A single crystal of SrTiO₃ slightly doped with La (0.075 wt%) was used to perform
 405 the experiments. The introduction of La as a dopant results in a small residual bulk conductivity that
 406 helps to avoid sample charging during the experiment. The crystal was cleaved in situ at the
 407 measurement temperature of $T = 15$ K in a pressure lower than 10^{-10} mbar. The surface was exposed
 408 to synchrotron light of 51 eV in order to saturate the bandwidth of the 2DEG³⁰. After this procedure
 409 ARPES measurements were taken using linear horizontal polarized photons with an energy of 51 eV.
 410 The combined energy resolution was ~ 20 meV. In the insets of Fig. 4 (a,b) we have enhanced the
 411 contrast by dividing the data by a smooth function of momentum. We verified that this procedure
 412 does not significantly change the position of peaks.

413 **Tight-binding model.** The Hamiltonian is a generalized version of that from Ref.³¹ We consider the
 414 two energetically lowest d_{xy} bands and one d_{yz} and d_{zx} band, respectively. The Hamiltonian includes
 415 spin, nearest-neighbor hopping (quantified by t, t_h), spin-orbit interaction (λ) and orbital mixing
 416 (g_1, g_2)

$$H = \begin{pmatrix} \epsilon_{xy1} & 0 & f_{1x} & f_{1y} & 0 & 0 & \lambda & -i\lambda \\ 0 & \epsilon_{xy2} & f_{2x} & f_{2y} & 0 & 0 & \lambda & -i\lambda \\ -f_{1x} & -f_{2x} & \epsilon_{yz} & i\lambda & -\lambda & -\lambda & 0 & 0 \\ -f_{1y} & -f_{2y} & -i\lambda & \epsilon_{zx} & i\lambda & i\lambda & 0 & 0 \\ 0 & 0 & -\lambda & -i\lambda & \epsilon_{xy1} & 0 & f_{1x} & f_{1y} \\ 0 & 0 & -\lambda & -i\lambda & 0 & \epsilon_{xy2} & f_{2x} & f_{2y} \\ \lambda & \lambda & 0 & 0 & -f_{1x} & -f_{2x} & \epsilon_{yz} & -i\lambda \\ i\lambda & i\lambda & 0 & 0 & -f_{1y} & -f_{2y} & i\lambda & \epsilon_{zx} \end{pmatrix},$$

417 with the diagonal elements

$$\begin{aligned} \epsilon_{xyj} &= 2t [2 - \cos(k_x) - \cos(k_y)] + o_j, \\ \epsilon_{yz} &= 2t [1 - \cos(k_y)] + 2t_h [1 - \cos(k_x)] + o_3, \end{aligned}$$

$$\epsilon_{zx} = 2t [1 - \cos(k_x)] + 2t_h [1 - \cos(k_y)] + o_3,$$

418 and the orbital mixing term

$$f_{jm} = 2ig_j \sin(k_m).$$

419 The parameters are:

$$\begin{aligned} t &= 0.388 \text{ eV}, t_h = 0.031 \text{ eV}, \\ o_1 &= -0.205 \text{ eV}, o_2 = -0.105 \text{ eV}, o_3 = -0.0544 \text{ eV}, \\ g_1 &= 0.002 \text{ eV}, g_2 = 0.005 \text{ eV}, \\ \lambda &= \frac{1}{120} \text{ eV}, \end{aligned}$$

420 resulting in a good agreement with the ARPES data (Fig. 4a-d).

421 **Calculation of the Edelstein effect.** The tensor for the Edelstein effect $\hat{\kappa}$ characterizes the spin
422 density per unit cell \mathbf{s} as a response to an externally applied electric field \mathbf{E}

$$\mathbf{s} = \hat{\kappa} \mathbf{E}.$$

423 It is calculated using the semi-classical Boltzmann transport theory,

$$\kappa_{ij} = \frac{-eA_0}{A} \sum_{\mathbf{k}} \langle \sigma \rangle_{\mathbf{k}}^i \Lambda_{\mathbf{k}}^j \delta(\epsilon_{\mathbf{k}} - \epsilon_F).$$

424 Here, A is the area of the system, A_0 is the area of the surface unit cell, $e > 0$ is the elementary
425 charge, and $\langle \sigma \rangle_{\mathbf{k}}$ is the spin expectation value of the state at wave vector \mathbf{k} and energy $\epsilon_{\mathbf{k}}$. The sum
426 is over all \mathbf{k} points and all bands. The mean free path $\Lambda_{\mathbf{k}} = \tau_0 \mathbf{v}_{\mathbf{k}}$ is approached by the constant
427 relaxation time approximation $\tau_0 = 1$ ps. At zero temperature, only states at the Fermi level ϵ_F
428 contribute to the Edelstein effect.

429 For the 2DEG Hamiltonian, symmetry only allows for nonzero tensor elements $\kappa_{xy} = -\kappa_{yx}$. Thus, an
430 external electric field induces an in-plane spin density perpendicular to the field, as in Rashba
431 systems.

432 **Poisson-Schrödinger calculations.** The electronic states of the carriers in the 2DEG were determined
433 with the help of the Poisson-Schrödinger algorithm which self-consistently yields the shape of the
434 electrostatic potential at the interface and the sub-band structure. For a set total electric charge
435 density, we solved the Schrödinger equation for a particle in a potential well, using values of the
436 effective masses corresponding to the hopping parameters t and t_h introduced in the tight-binding
437 model. We also include the atomic spin-orbit coupling in our computation, described by the

438 parameter λ in the tight-binding Hamiltonian. From the eigenfunctions and eigenenergies of the
439 Schrödinger equation one obtains the density profile and then solving Poisson equation gives the
440 spatial dependence of the electrostatic potential in the material. The procedure is then iterated until
441 self-consistency is achieved.

442 REFERENCES

- 443 1. Bychkov, Y. A. & Rashba, E. I. Properties of a 2D electron gas with lifted spectral degeneracy.
444 *JETP Lett.* **39**, 78–81 (1984).
- 445 2. Manchon, A., Koo, H. C., Nitta, J., Frolov, S. M. & Duine, R. A. New perspectives for Rashba
446 spin–orbit coupling. *Nature Mater.* **14**, 871–882 (2015).
- 447 3. Edelstein, V. M. M. Spin polarization of conduction electrons induced by electric current in
448 two-dimensional asymmetric electron systems. *Solid State Commun.* **73**, 233–235 (1990).
- 449 4. Rojas-Sánchez, J. C. *et al.* Spin-to-charge conversion using Rashba coupling at the interface
450 between non-magnetic materials. *Nature Commun.* **4**, 2944 (2013).
- 451 5. Rojas-Sánchez, J.-C. *et al.* Spin to Charge Conversion at Room Temperature by Spin Pumping
452 into a New Type of Topological Insulator: α -Sn Films. *Phys. Rev. Lett.* **116**, 096602 (2016).
- 453 6. Han, W., Otani, Y. & Maekawa, S. Quantum materials for spin and charge conversion. *npj*
454 *Quantum Mater.* **3**, 27 (2018).
- 455 7. Johansson, A., Henk, J. & Mertig, I. Edelstein effect in Weyl semimetals. *Phys. Rev. B* **97**,
456 085417 (2018).
- 457 8. Zhang, S. & Fert, A. Conversion between spin and charge currents with topological insulators.
458 *Phys. Rev. B* **94**, 184423 (2016).
- 459 9. Shen, K., Vignale, G. & Raimondi, R. Microscopic Theory of the Inverse Edelstein Effect. *Phys.*
460 *Rev. Lett.* **112**, 096601 (2014).
- 461 10. Lesne, E. *et al.* Highly efficient and tunable spin-to-charge conversion through Rashba
462 coupling at oxide interfaces. *Nature Mater.* **15**, 1261–1266 (2016).
- 463 11. Seibold, G., Caprara, S., Grilli, M. & Raimondi, R. Theory of the Spin Galvanic Effect at Oxide
464 Interfaces. *Phys. Rev. Lett.* **119**, 256801 (2017).
- 465 12. Ohtomo, A. & Hwang, H. Y. A high-mobility electron gas at the LaAlO₃/SrTiO₃ heterointerface.
466 *Nature* **427**, 423–6 (2004).
- 467 13. Caviglia, A. D. *et al.* Electric field control of the LaAlO₃/SrTiO₃ interface ground state. *Nature*
468 **456**, 624–7 (2008).
- 469 14. Thiel, S., Hammerl, G., Schmehl, A., Schneider, C. W. & Mannhart, J. Tunable quasi-two-
470 dimensional electron gases in oxide heterostructures. *Science* **313**, 1942–1945 (2006).

- 471 15. Lesne, E. *et al.* Suppression of the critical thickness threshold for conductivity at the
472 LaAlO₃/SrTiO₃ interface. *Nature Commun.* **5**, 4291 (2014).
- 473 16. Vaz, D. C. *et al.* Tuning Up or Down the Critical Thickness in LaAlO₃/SrTiO₃ through In Situ
474 Deposition of Metal Overlayers. *Adv. Mater.* **29**, 1700486 (2017).
- 475 17. Rödel, T. C. *et al.* Universal Fabrication of 2D Electron Systems in Functional Oxides. *Adv.*
476 *Mater.* **28**, 1976–1980 (2016).
- 477 18. Posadas, A. B. *et al.* Scavenging of oxygen from SrTiO₃ during oxide thin film deposition and
478 the formation of interfacial 2DEG. *J. Appl. Phys.* **105302**, (2017).
- 479 19. Sing, M. *et al.* Profiling the Interface Electron Gas of LaAlO₃/SrTiO₃ Heterostructures with Hard
480 X-Ray Photoelectron Spectroscopy. *Phys. Rev. Lett.* **102**, 176805 (2009).
- 481 20. Hurand, S. *et al.* Field-effect control of superconductivity and Rashba spin-orbit coupling in
482 top-gated LaAlO₃/SrTiO₃ devices. *Sci. Rep.* **5**, 12751 (2015).
- 483 21. Tserkovnyak, Y., Brataas, A. & Bauer, G. E. W. Enhanced gilbert damping in thin ferromagnetic
484 films. *Phys. Rev. Lett.* **88**, 117601 (2002).
- 485 22. Rojas-Sánchez, J.-C. *et al.* Spin pumping and inverse spin Hall effect in germanium. *Phys. Rev.*
486 *B* **88**, 064403 (2013).
- 487 23. Pham, V. T. *et al.* Ferromagnetic/Nonmagnetic Nanostructures for the Electrical Measurement
488 of the Spin Hall Effect. *Nano Lett.* **16**, 6755–6760 (2016).
- 489 24. Noel, P. *et al.* Highly Efficient Spin-to-Charge Current Conversion in Strained HgTe Surface
490 States Protected by a HgCdTe Layer. *Phys. Rev. Lett.* **120**, 167201 (2018).
- 491 25. Mendes, J. B. S. *et al.* Dirac-surface-state-dominated spin to charge current conversion in the
492 topological insulator (Bi_{0.22}Sb_{0.78})₂Te₃ films at room temperature. *Phys. Rev. B* **96**, 180415
493 (2017).
- 494 26. Karube, S., Kondou, K. & Otani, Y. Experimental observation of spin-to-charge current
495 conversion at non-magnetic metal/Bi₂O₃ interfaces. *Appl. Phys. Express* **9**, 033001 (2016).
- 496 27. King, P. D. C. *et al.* Quasiparticle dynamics and spin-orbital texture of the SrTiO₃ two-
497 dimensional electron gas. *Nature Commun.* **5**, 3414 (2014).
- 498 28. Zhong, Z., Tóth, A. & Held, K. Theory of spin-orbit coupling at LaAlO₃/SrTiO₃ interfaces and
499 SrTiO₃ surfaces. *Phys. Rev. B* **87**, 161102 (2013).

- 500 29. Khalsa, G. & MacDonald, A. H. Theory of the SrTiO₃ surface state two-dimensional electron
501 gas. *Phys. Rev. B* **86**, 125121 (2012).
- 502 30. McKeown Walker, S. *et al.* Carrier-Density Control of the SrTiO₃ (001) Surface 2D Electron Gas
503 studied by ARPES. *Adv. Mater.* **27**, 3894–3899 (2015).
- 504 31. Vivek, M., Goerbig, M. O. & Gabay, M. Topological states at the (001) surface of SrTiO₃. *Phys.*
505 *Rev. B* **95**, 165117 (2017).
- 506 32. Zhong, Z., Tóth, A. & Held, K. Theory of spin-orbit coupling at LaAlO₃/SrTiO₃ interfaces and
507 SrTiO₃. *Phys. Rev. B* **87**, 161102 (2013).
- 508 33. Kim, J. *et al.* Evaluation of bulk-interface contributions to Edelstein magnetoresistance at
509 metal/oxide interfaces. *Phys. Rev. B* **96**, 140409 (2017).
- 510 34. Dey, R., Prasad, N., Register, L. F. & Banerjee, S. K. Conversion of spin current into charge
511 current in a topological insulator: Role of the interface. *Phys. Rev. B* **97**, 174406 (2018).
- 512 35. Herranz, G. *et al.* High Mobility in LaAlO₃/SrTiO₃ Heterostructures: Origin, Dimensionality, and
513 Perspectives. *Phys. Rev. Lett.* **98**, 216803 (2007).
- 514 36. Manipatruni, S. *et al.* Scalable energy-efficient magnetoelectric spin–orbit logic. *Nature* **565**,
515 35–42 (2019).
- 516 37. Manipatruni, S., Nikonov, D. E. & Young, I. A. Beyond CMOS computing with spin and
517 polarization. *Nature Phys.* **14**, 338–343 (2018).
- 518 38. Varignon, J., Vila, L., Barthélémy, A. & Bibes, M. A new spin for oxide interfaces. *Nature Phys.*
519 **14**, 322–325 (2018).
- 520 39. Xiao, D., Zhu, W., Ran, Y., Nagaosa, N. & Okamoto, S. Interface engineering of quantum Hall
521 effects in digital transition metal oxide heterostructures. *Nature Commun.* **2**, 596 (2011).
- 522